Cellulose crystals plastify by localized shear

Gergely Molnár[a], David Rodney[b], Florian Martoïa[c], Pierre J. J. Dumont[c], Yoshiharu Nishiyama[d], Karim Mazeau[d], and Laurent Orgéas[a,1]

[a]Université Grenoble Alpes, CNRS, Grenoble Institute of Technology, Laboratoire Sols, Solides, Structures, Risques, F-38000 Grenoble, France; [b]Université de Lyon, CNRS, Institut Lumière Matière, F-69622 Villeurbanne, France; [c]Université de Lyon, Institut National des Sciences Appliquées de Lyon, CNRS, Laboratoire de Mécanique des Contacts et des Structures, F-69621 Lyon, France; and [d]Université Grenoble Alpes, CNRS, Centre de Recherche sur les Macromolécules Végétales, F-38000 Grenoble, France

Cellulose microfibrils are the principal structural building blocks of wood and plants. Their crystalline domains provide outstanding mechanical properties. Cellulose microfibrils have thus a remarkable potential as eco-friendly fibrous reinforcements for structural engineered materials. However, the elastoplastic properties of cellulose crystals remain poorly understood. Here, we use atomistic simulations to determine the plastic shear resistance of cellulose crystals and analyze the underpinning atomic deformation mechanisms. In particular, we demonstrate how the complex and adaptable atomic structure of crystalline cellulose controls its anisotropic elastoplastic behavior. For perfect crystals, we show that shear occurs through localized bands along with noticeable dilatancy. Depending on the shear direction, not only noncovalent interactions between cellulose chains but also local deformations, translations, and rotations of the cellulose macromolecules contribute to the response of the crystal. We also reveal the marked effect of crystalline defects like dislocations, which decrease both the yield strength and the dilatancy, in a way analogous to that of metallic crystals.

crystalline cellulose | nanoscale plasticity | shear bands | dislocations | molecular mechanics simulation

ENGINEERING

Wood and bamboo have been used as structural materials since ancient times due to their lightweight and remarkable mechanical properties. One of the elementary building blocks at the origin of these properties is cellulose microfibrils (1, 2) that are few-nanometer–thick slender fibers with a continuous crystalline core produced at the cell membrane by the simultaneous elongation and crystallization of cellulose chains. The large tensile modulus and strength of cellulose microfibrils make them potential biosourced alternatives to synthetic nanofibers as mechanical reinforcements (3, 4).

Vast research efforts are currently underway worldwide to extract from biomass slender crystalline cellulose nanoparticles (CNs) (2), i.e., portions of microfibrils. CNs are used as building blocks for novel engineered materials, such as nanocomposites (2, 3, 5), densely packed nanopapers (6–9) and filaments (10, 11) with tunable supermolecular nanostructures (12, 13), and aerogels and foams (14–16). However, during extraction, processing, and use, CNs are subjected to complex stress environments that alter their morphology and mechanical properties. For example, extraction routes often bend CNs, leading to the formation of detrimental kinks (17), which result from the bulk plastic deformation of cellulose crystals via localized shear processes (18). A better control of such phenomena requires a deeper knowledge of the mechanical behavior of CNs, which is linked to both their surface properties (19) and the bulk elastoplastic properties of their crystalline structure. The present work focuses on the latter aspect.

The structure of cellulose crystals (1, 20, 21) implies a highly anisotropic stiffness tensor, which so far has not been fully evaluated experimentally. Much attention was devoted to the longitudinal elastic modulus, estimated to be close to 150 GPa (22–24). The transverse tensile modulus was found to be much

smaller, on the order of 15 GPa (22, 25). The full stiffness tensor of cellulose crystals was estimated numerically, using quantum (26) and classical (27, 28) atomistic calculations. Transverse shear moduli were found to be 100 times smaller than longitudinal tensile moduli, indicating that shear could be the preferred mode of elastic deformation of cellulose crystals. Even in native conditions, these values are of the same order of magnitude as the shear stiffness of the amorphous matrix made of hemicellulose and lignin [1–3 GPa (29)]. It is therefore expected that cellulose crystals deform by shear in the plant cell walls as well.

However, very little is known about the mechanical behavior of cellulose crystals beyond the elastic domain. The mean longitudinal tensile strength of wood CNs was estimated experimentally to be between 1.6 GPa and 3 GPa (4). Atomistic simulations (30) found a value of ≈6 GPa, closer to that estimated from the strength of C-O bonds (30). The reason is probably that experimental CNs contain defects (17, 21, 31) that were not included in the simulations. Local shear deformation was analyzed with molecular dynamics (8) by pulling out a single cellulose chain from its crystal, but the intrinsic bulk shear resistance of a cellulose crystal still remains unknown and many questions are still open to form a complete and clear understanding of the elastoplastic shear deformation of cellulose crystals: (i) What is the overall stress–strain response of cellulose crystals? Do cellulose crystals deform homogeneously, anisotropically, with or without volume variation? (ii) What are the involved nanoscale mechanisms? Do they depend on the shearing orientation with respect to the crystal structure? And

---

Significance

While most attention has so far been devoted to the tensile properties of crystalline cellulose, the main elementary building block of plants, we show here using atomistic simulations that their shear is also an important mode of deformation, occurring at stress levels lower than tension with much larger ductility. We also demonstrate how crystalline defects like dislocations drastically facilitate plasticity. This analysis can be used as a basis for the micromechanical modeling of cellulose microfibrils that are currently considered as promising eco-friendly alternatives to synthetic fibers for structural materials.

(*iii*) do crystalline defects like dislocations affect the mechanical behavior of cellulose crystals as in crystalline metals?

To bring possible answers to the aforementioned questions and form a better view on the mechanics of cellulose crystals, we performed a comprehensive mechanical analysis of the interplay between the molecular structure and the shear elastoplastic response of cellulose crystals, using atomic-scale simulations. To that end, molecular mechanics simulations were carried out on cellulose I_β, the most common crystalline form of cellulose in plants and animals (20, 32). The corresponding atomic structure, sketched in Fig. 1 (see *SI Appendix*, section S1 for details), was modeled using a force field commonly used for carbohydrates (33, 34). Cellulose chains adopt an extended twofold helical conformation with a long axis c parallel to the z direction of the cell. They bond with each other by hydrogen bonds in the y direction, forming sheets of cellulose chains. As illustrated in Fig. 1D, cellulose chains are stacked along the x direction in a staggered manner and form a layered architecture visible in Fig. 1 *A* and *B*. We studied the mechanical response of periodic cellulose crystals subjected to finite simple shear strains along three different directions, which mainly involve weak nonbonded interchain interactions rather than the much stiffer intrachain covalent bonds. Hence, these directions are expected to be privileged directions of deformation. The crystals were thus sheared parallel to the cellulose layers to force cellulose chains to slide along their faces either perpendicularly (*xy* shear in Fig. 1*A*) or parallel (*xz* shear in Fig. 1*B*) to their long axis. We also sheared the crystals perpendicularly to the layers (*yz* shear in Fig. 1*C*), to induce sliding of the chains along their side. This shear direction corresponds to the pull-out direction investigated in ref. 8. While so far only perfect crystals have been considered numerically, we also sheared a crystal containing defects akin to dislocations (35) to highlight their influence on the global stress response.

Elastoplastic Shear Deformation of Perfect Crystals

Fig. 2 *A–C* shows the shear stress/shear strain curves obtained with perfect I_β crystals for the three considered shear directions. All curves start by a linear elastic regime where the crystal deformation is homogeneous with shuffles inside the unit cells (see *SI Appendix*, section S3 for details) and with $G_{xy} = 2.40$ GPa, $G_{xz} = 2.43$ GPa, and $G_{yz} = 16.37$ GPa, in agreement with ab initio estimations (26). The shear stress then exhibits a nonlinear increase up to a maximum, namely the ideal shear strength (36–38), which is the maximum shear stress the perfect crystal can sustain. Ideal shear strengths follow the same order as shear moduli: $\tau_{xy}^{max} = 0.39$ GPa and $\tau_{xz}^{max} = 0.48$ GPa are close, while $\tau_{yz}^{max} = 1.65$ GPa is about five times larger. They are smaller but of the same order of magnitude as the ultimate stresses estimated during tensile loading (30). Moreover, while the tensile elongation at failure of cellulose crystals is limited to a few percent

due to decohesion between cellulose chains or breaking of C-O covalent bonds (30), Fig. 2 shows that the shear ductility of perfect crystals is without bounds. Also, Fig. 2 *D–F* shows that before the first stress drop, cellulose crystals expand anisotropically and perpendicularly to the cellulose layers by up to 7%. This marked dilatancy reflects that cellulose chains need to separate before they can slide over one another (see *Related Atomic-Scale Mechanisms*). Other similar dilatant mechanisms are known for instance in wood (39), polymers (40), collagen networks (41), granular media (42), and entangled fibrous materials (43).

Besides these general trends, the elastoplasticity of cellulose crystals was strongly affected by the shearing direction. Stress results depicted in Fig. 2*A* show that, when the sample is sheared in the *xy* plane, the stress follows a long plateau beyond the ideal shear strength before dropping abruptly. At this point, the deformation localizes between cellulose layers to form shear bands that span the entire length of the simulation cell. As illustrated in Fig. 2*A*, *Inset* and Movie S1, two shear bands coexist but this number depends on numerical noise. The shear bands form between layers of cellulose ribbons and allow one layer to slide over the other to recover a perfect crystal. As a result, the stress drops close to zero. The slightly negative remaining stress is due to an elastic deformation of the otherwise perfect crystal. The offset inside a shear band corresponds to the unit cell parameter b in the y direction. The strain where a perfect undeformed crystal is recovered depends on this parameter but also on the number of shear bands ($n = 2$) and the height of the simulation box in the z direction ($h = 2.30$ nm) as $\gamma_{xy} = nb/h = 0.698$, which is exactly the strain in Fig. 2*A* where the stress is back to zero. If the applied strain was increased from this point, the stress/strain curve would repeat itself periodically. The capacity of the crystal to fully recover is due to the high adaptability of the noncovalent, long-range interactions between cellulose layers, which physically represent London dispersion interactions.

Shear bands between cellulose layers also form when the crystal is sheared in the *xz* plane. As seen in Fig. 2*B*, the yielding process now involves three stress drops, which will be analyzed from the atomic-scale structure of the crystals below. As illustrated in Fig. 2*B*, *Inset* and in Movie S2, two shear bands form again and a perfect crystal is recovered when the sliding distance between chains in the z direction reaches the crystal parameter c. The corresponding strain is $\gamma_{xz} = 2c/h = 0.9$, which is again the strain where in Fig. 2*B* the stress is exactly zero and a perfect undeformed crystal is recovered.

Finally, shear elastoplasticity in the *yz* plane is more complex and requires larger shear stresses. Here, in contrast with the first two orientations, hydrogen bonds between cellulose chains are involved. The stress–strain curve shown in Fig. 2*C* contains both small and large stress drops. Large drops are connected to
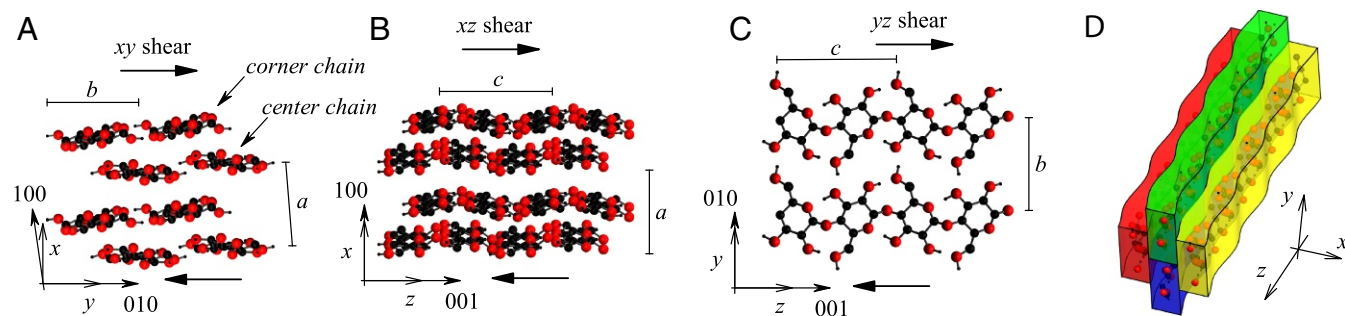

Fig. 1. Atomic structure of I_β cellulose. From *Left* to *Right*, molecular chains are shown in the *xy* (A), *xz* (B), and *yz* (C) planes. The direction of the applied shear strain is shown in each case. *D* is a 3D geometrical volume fitted on the cellulose chains to highlight their corrugation. Three-dimensional interactive representations are shown in *SI Appendix*, Figs. S2 and S3. (The hydrogen atoms bonded to carbon atoms are not shown here.)
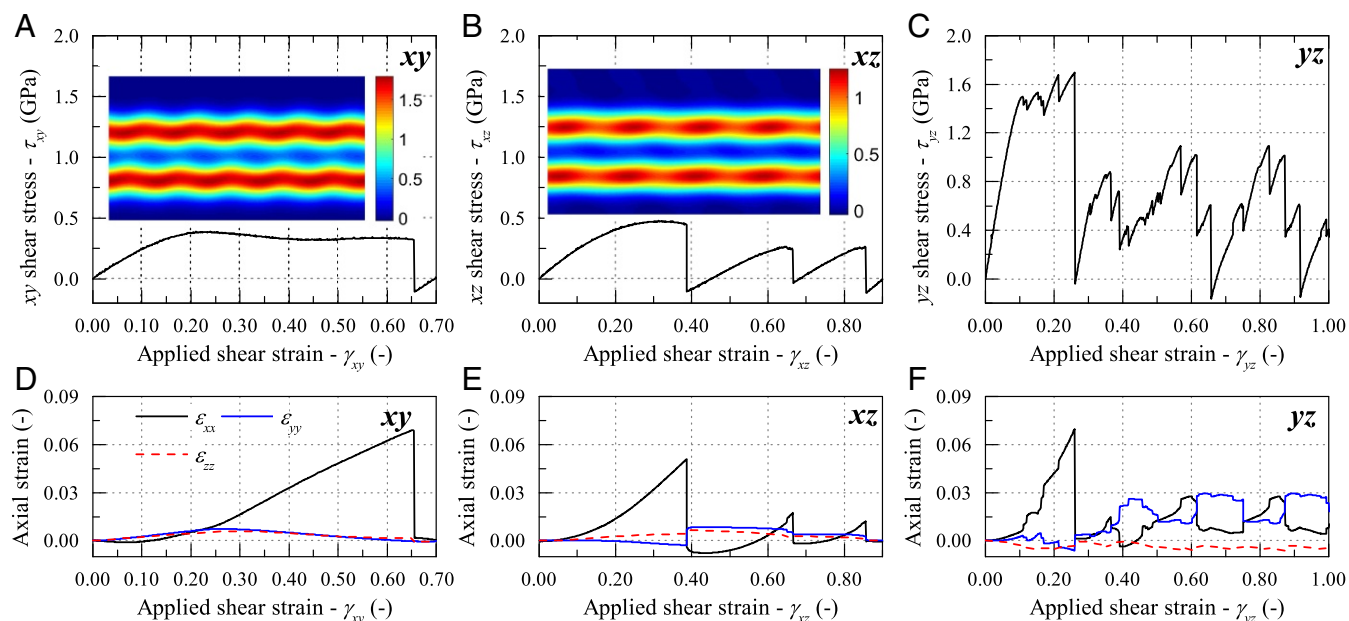
Fig. 2. Shear deformation in different planes. (*A–C*) Shear stress–strain curves in the *xy*, *xz*, and *yz* planes. (*D–F*) Corresponding axial strains. Atomic-scale deformation mechanisms are shown in Movies S1–S3. In *A* and *B*, *Insets*, the local coarse-grained shear strain is shown just after the first plastic event.

localized shear bands between cellulose ribbons, whereas smaller drops are due to more localized irreversible events along the molecules (see *Related Atomic-Scale Mechanisms*). Also, we see in Fig. 2*C* that the first large yield event, which occurs at $\gamma_{yz} \approx 0.25$, is not equivalent to the following deformation cycles.

Related Atomic-Scale Mechanisms

We now investigate the atomic-scale origins of shear elastoplasticity in cellulose crystals and consider first shear in the *xy* plane. As shown in Fig. 1*A*, there are two crystallographically independent chain types, the so-called corner and center chains. The cellulose chains are not parallel to the *y* direction but are slightly tilted around their helical axis with respective angles of $\approx 12°$ and $\approx -16°$ (measured from the angles of the pyran mean planes shown in Fig. 3*A*).

This misorientation induces steric effects that include a sliding resistance between chains and the crystal expansion ε_{xx} seen in Fig. 2*D*. In addition, as the sample is sheared, Fig. 3*A* and Movie S4 show that center and corner chains tend to align, thus leading to a decrease of the interchain roughness: The center chain angle increases to $+7°$ while the corner chain angle decreases to $9°$. These rotations occur during the stress plateau in Fig. 2*A*. They cause a loss of the crystal stiffness and allow the layers to slide more easily. Interestingly, if the deformation is reversed at this stage (Fig. 3*B*), the chains rotate back and the stress–strain curve is reversible within numerical accuracy, showing that cellulose crystals behave as hyperelastic media up to the plastic instability. At the end of the plateau, plastic deformation occurs. The chains regain their initial environment, up to a rigid shift, in a perfect crystal and the initial tilts are recovered, as seen in Fig. 3*A*, *Right*.

To highlight the atomic-scale rearrangements in the *xz* plane, we intentionally induced a single shear band in the crystal (see *SI Appendix*, section S5 for details). The result is analyzed in Fig. 4. To follow the motion of cellulose molecules, we use the relative *z* position of a reference carbon atom in one glucose residue of the top layer ($C3^T$) with respect to the two equivalent carbon atoms ($C3^1$ and $C3^2$) in glucose units of the bottom chain (see glucose molecule in *SI Appendix*, Fig. S1 for details). Upon shear, the distance between the C3 atoms decreases (Fig.

4) until at $\gamma_{xz} = 0.32$, the upper $C3^T$ and the first lower $C3^1$ atoms are almost aligned vertically. This is an unstable position of strong repulsion between layers, which reach a maximum separation (Fig. 2*E*). The separation is enhanced by the corrugated shape of the cellulose chains in the *z* direction. Unloading the crystal before this point is reversible as when shearing in the *xy* plane (see Fig. 6*C*). Conversely, loading the crystal beyond
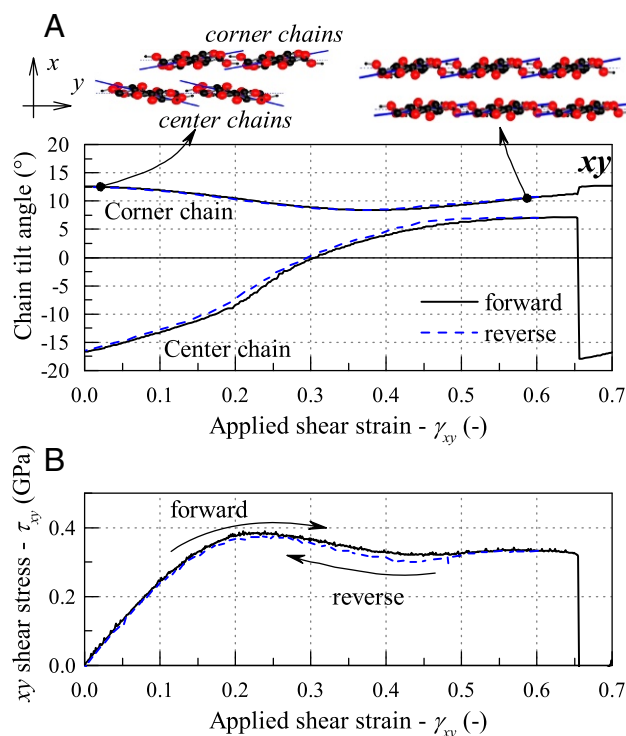

Fig. 3. Evolution of chain tilt angles in the *xy* plane as a function of shear strain (*A*) and corresponding forward and reverse stress/strain curves (*B*). Atomic-scale deformation is shown in Movie S4.
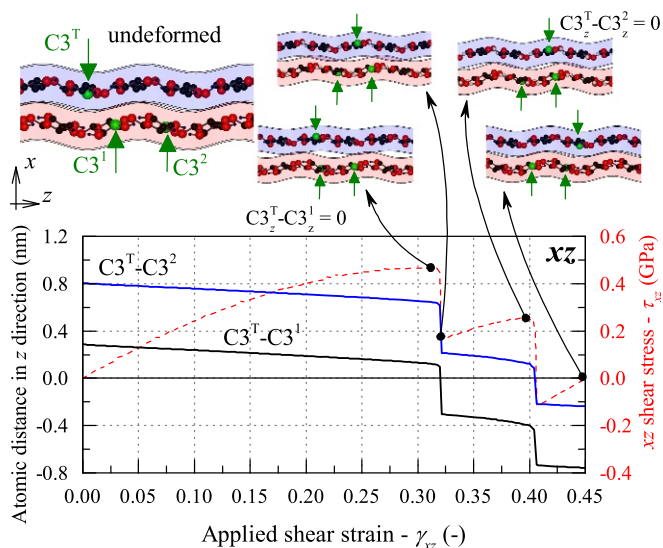
Fig. 4. Relative position of the corrugated cellulose chains during shear in the *xz* plane. The blue and black curves show the distance in the *z* direction between a reference carbon atom in an upper chain, $C3_3^T$, and two carbon atoms, $C3_3^i$ with $i = 1, 2$ in a lower chain. The stress–strain curve is in red. Molecular-level deformation is shown in Movie S5.

the unstable position induces a first plastic event: Both ribbons slide discontinuously by about $\Delta d = 0.4$ nm to reach a new metastable position. The corresponding stress drop, $\Delta \tau_{xz} \approx 0.38$ GPa, can be calculated from the plastic strain generated during the event, $\gamma_{xz}^{pl} = \Delta d/h$, as $\Delta \tau_{xz} = G_{xz}\gamma_{xz}^{pl}$, where $G_{xz} = 2.03$ GPa is the shear modulus computed just after yield drop (44). This first yield event is followed by a second elastic regime (between $\gamma_{xz} = 0.32$ and 0.41) until $C3^T$ aligns with $C3^2$. Glucose molecules again overlap, leading to a second yield event similar to the first one. Finally, between $\gamma_{xz} = 0.41$ and 0.45, the crystal is deformed elastically to recover its perfect undeformed structure at $\gamma_{xz} = 0.45$. The sliding mechanism is further demonstrated in Movie S5. Yielding in the *xz* plane therefore involves two successive plastic events, which correspond to the successive sliding of glucose molecules on top of each other. There are three stress drops in Fig. 2*B* because two shear bands formed in this case and while the first yield event occurred simultaneously in both bands, the second did not, leading to two smaller drops.

Finally, when cellulose crystals are sheared in the *yz* plane, Fig. 5*A* shows that the shear band is not flat, but zigzags between cellulose ribbons, reflecting the staggered stacking of the cellulose molecules in the *x* direction (Fig. 1 *A* and *D*). In this

situation, not only the wavy shape of cellulose chains and the London dispersion interactions between molecules are involved, but also hydrogen bonds between chains. These combined effects probably result in the much larger shear strength than with previous orientations (Fig. 2*C*). Moreover, Fig. 5*B* shows the O5-C5-C6-O6 dihedral angle of two sliding molecules, before and after the first yield event. We see that the dihedral angle on the top molecule flips from $157°$ to $63°$ during the plastic event, as evidenced at the atomic scale in Fig. 5 *C* and *D*. This change of conformation of the molecule affects the hydrogen bonds with the lower glucose molecule in the shear band and allows for an easier sliding, as attested by the lower stresses seen in Fig. 2*C* after the first yield event. This dihedral rotation is also visible in the work of Zhu et al. (8) but not mentioned. The mechanism of breaking and reformation of hydrogen bonds between the cellulose chains is further illustrated in Movie S6. Finally, note that the *yz* shear induces a noticeable expansion strain ε_{xx} perpendicular to the cellulose layers, as large as ε_{yy} (Fig. 2*F*). Such strain again results from the relative motion of the cellulose chains, which have a corrugated shape along this direction (Fig. 1*B*).

Effect of Dislocations

So far, we have considered perfect cellulose crystals. However, cellulose microfibrils are grown from natural processes and the crystals are expected to contain atomic-scale defects, such as vacancies and dislocations, although the latter are difficult to observe experimentally. As a first approach to study the impact of defects on the mechanics of cellulose crystals, we consider here dislocations in the *xz* plane because they induce sliding of cellulose layers along their long axis, which is the major deformation mode involved in the formation of kinks on CNs (18).

As proposed for metallic crystals (45), we introduced two edge dislocations between cellulose layers in the *xz* plane to form a dipole with opposite *c* Burgers vectors, as sketched in Fig. 6*A*. In Fig. 6*B*, *Insets* show that around the dislocations, cellulose chains are deformed from a large corrugation in the compressive side of the extra half plane of the dislocations to an almost flat state in the tension side.

When shearing the dislocated crystal (Fig. 6*C*), we find first that the dislocations do not alter the initial linear elastic regime. The dislocations start to glide and induce plastic deformation at a critical stress, which we call Peierls stress in analogy with metallic crystals (46), of about 0.29 GPa, i.e., much lower than the ideal shear strength (0.48 GPa). The crystal deformation then occurs at constant stress, in contrast with the marked stress drops seen with perfect crystals. As shown in *SI Appendix*, Fig. S8, the crystal deformation is localized in the dislocation planes, and as in metallic crystals (46), dislocation motion requires only local rearrangements and therefore less stress than shearing two
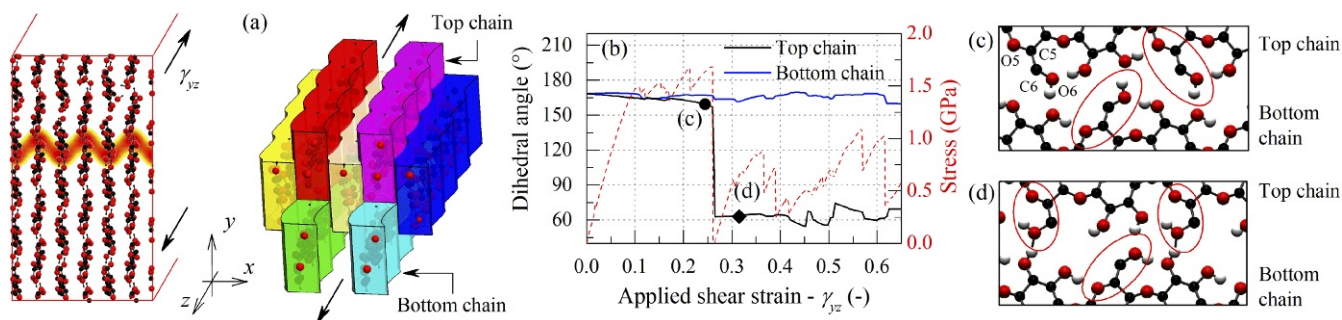

Fig. 5. (*A*) Coarse-grained shear strain map in projection perpendicular to the shear direction (in the *xy* plane) with a 3D sketch of the molecular structure and orientation of the applied shear strain. (*B*) O5-C5-C6-O6 dihedral angles of the chains shown in *C* and *D* in the shear band as a function of applied deformation. (*C* and *D*) Local atomic structure before (*C*) and after (*D*) the first large stress drop.
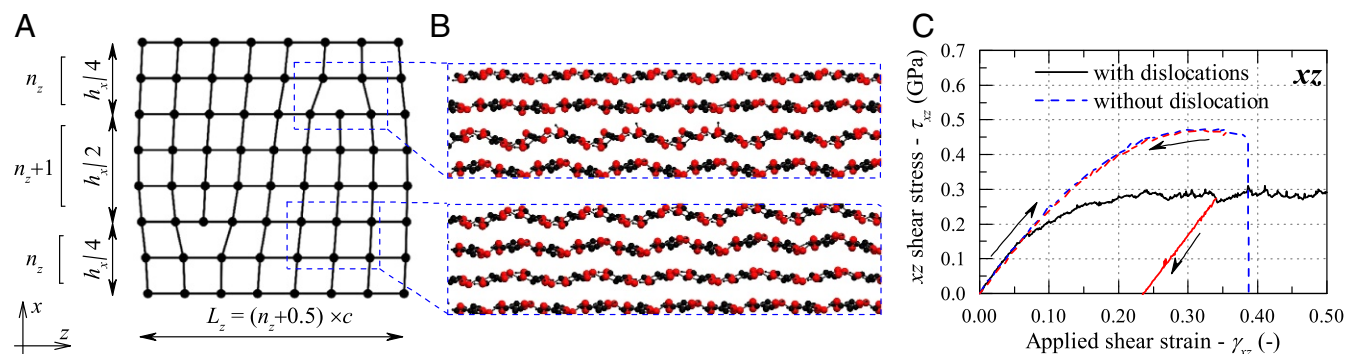
Fig. 6. Shear in the *xz* plane in the presence of two edge dislocations forming a dipole. A schematic representation of the dislocated crystal is shown in *A*, and details of the molecular structure near and far from a dislocation core are shown in *B*. The resulting stress–strain curve is compared with that of a perfect crystal in *C*.

entire adjacent layers. In addition, most of the lattice changes are located in the vicinity of the dislocations, thus reducing the overall volume change of the crystal down to 0.8% for the present dislocated crystal configuration and size. Finally, while in perfect crystals the behavior is fully reversible up to the first stress drop, we see in Fig. 6*C* that unloading the dislocated crystals leads to noticeable plastic strains as soon as the linear elastic domain ends, a consequence of irreversibility of dislocation glide.

Concluding Remarks

Enhancing our knowledge on the mechanics of CNs is essential before we can use them as building blocks in structural materials. This is crucial beyond the elastic domain where the literature is still scarce. To that end, we focused on the bulk shear plasticity of I_β cellulose crystals. In response to the questions listed in the Introduction, we state the following:

i) Stress–strain response: Shearing perfect crystals beyond linear elasticity is highly nonlinear and anisotropic. The crystal response is composed of periodic sequences of hyperelastic branches followed by abrupt plastic events. The associated ideal shear stresses, in the range of 0.4–1.65 GPa, are lower than the ultimate tensile strengths reported previously (4, 30). Thus, as for elasticity, shear plasticity should be a preferred deformation mode in many situations. In addition, shear ductility is not limited because interchain interactions can reform after a shear event while they cannot when broken in tension (30). Such ductility may be one of the sources of toughness of CN-based materials such as nanopapers (8).

ii) Nanoscale deformation mechanisms: Shear plasticity proceeds by shear bands between cellulose layers, along with noticeable dilatancy. Zooming in at the atomic scale showed that, while continuously breaking and reforming, hydrogen bonds and London dispersion forces contribute very efficiently to the crystal shear strength and ductility. The role of hydrogen bonds was recently highlighted for shear in the *yz* plane (8), while that of London dispersion forces has so far been largely overlooked in cellulose (47). Also, we found that the layered and staggered architecture of the cellulose chains, as well as their internal deformation, are paramount for the crystal plasticity and related dilatancy.

iii) Effect of crystal defects: Although their occurrence still needs to be confirmed experimentally, we demonstrated the drastic changes induced by defects like dislocations. Dislocated cellulose exhibits an elastoplastic behavior similar to that of metallic crystals, with a short linear elastic domain and lower flow stress and volume variation, without abrupt stress drops.

Obviously, additional investigations are needed to better understand the plasticity of CNs. Among them, the effect of the crystal finite size and environment should be further examined to unveil size and surface effects. Anyway, results presented in the literature in tension (30) and in this work in shear already constitute a suitable base to build beam models (43) for the bulk mechanics of CNs beyond elasticity in the context of a multiscale approach.

Materials and Methods

Initial Structure. The simulations were performed using the GROMACS package version 5.1. (48), a modified Gromos 56A$_{carbo}$ force field (33, 34) (see *SI Appendix*, section S2 for details on the choice of force field), and periodic boundary conditions. I_β cellulose crystals were generated from the atomic structure measured experimentally (20). Water was not considered here since it does not penetrate in cellulose crystals (49). Molecular dynamics simulations at 300 K were used to equilibrate the samples, first at constant volume for 1 ns and then at constant pressure (1 bar) for another 1 ns. The samples were then quenched at ambient pressure to 0 K and relaxed with conjugate gradient to produce equilibrium configurations. The final unit cell has dimensions $a = 0.7681$ nm, $b = 0.8027$ nm, $c = 1.0387$ nm, $\alpha = \beta \cong 90°$, and $\gamma = 92.8°$. The simulated crystals were mainly made of $3a \times 55b \times 44c$ unit cells and contained 3,360 atoms. We checked that results did not depend on the cell size (see *SI Appendix*, section S4 for details). The dislocated crystals were larger, $32a \times 55b \times 1,616c$, with about 150,000 atoms (see *SI Appendix*, section S6 for details).

Deformation. I_β cellulose crystals were deformed quasi-statically using molecular mechanics. At each deformation step, the simulation cell was sheared, with the atomic positions rescaled homogeneously, and a new equilibrium configuration was obtained by a conjugate gradient energy minimization. The incremental shear strain $\delta\gamma$ was set to 10^{-3}, as detailed in ref. 50. The shear deformations were applied at zero normal stresses. Hence, tensile stresses induced during each shear step were relaxed by changing the cell dimensions based on the elastic stiffnesses of the crystals. If the resulting tensile stresses remained larger than 0.03 GPa (which occurred only after large shear stress drops), the normal stresses were relaxed to zero using a barostat before a new shear increment was applied. Finally, to produce continuous strain fields after the simulations, a coarse-graining representation was used: Atomic displacements were convoluted with a Gaussian function of width 0.3 nm, as detailed in *SI Appendix*, section S3 and in ref. 51. The quantitative values of the local strain field depend on the coarse-graining width, but not the localization patterns seen in Figs. 2 and 5. The effect of the coarse-graining width is further analyzed in *SI Appendix*, section S3.

ENGINEERING

1. Fernandes AN, et al. (2011) Nanostructure of cellulose microfibrils in spruce wood. *Proc Natl Acad Sci USA* 108:E1195–E1203.
2. Moon RJ, Martini A, Nairn J, Simonsen J, Youngblood J (2011) Cellulose nanomaterials review: Structure, properties and nanocomposites. *Chem Soc Rev* 40:3941–3994.
3. Dufresne A, ed (2018) *Nanocellulose: From Nature to High Performance Tailored Materials* (Walter de Gruyter, Berlin), 2nd Ed.
4. Saito T, Kuramae R, Wohlert J, Berglund L, Isogai A (2013) An ultrastrong nanofibrillar biomaterial: The strength of single cellulose nanofibrils revealed via sonication-induced fragmentation. *Biomacromolecules* 14:248–253.
5. Abdul Khalil HPS, Bhat AH, Ireana Yusra AF (2012) Green composites from sustainable cellulose nanofibrils: A review. *Carbohydr Polym* 87:963–979.
6. Benítez AJ, Torres-Rendon J, Poutanen M, Walther A (2013) Humidity and multiscale structure govern mechanical properties and deformation modes in films of native cellulose nanofibrils. *Biomacromolecules* 14:4497–4506.
7. Bardet R, Belgacem M, Bras J (2015) Flexibility and color monitoring of cellulose nanocrystal iridescent solid films using anionic or neutral polymers. *ACS Appl Mater Interfaces* 7:4010–4018.
8. Zhu H, et al. (2015) Anomalous scaling law of strength and toughness of cellulose nanopaper. *Proc Natl Acad Sci USA* 112:8971–8976.
9. Martoïa F, Dumont P, Orgéas L, Belgacem M, Putaux JL (2016) On the origins of the elasticity of cellulose nanofiber nanocomposites and nanopapers: A micromechanical approach. *RSC Adv* 16:47258–47271.
10. Håkansson KMO, et al. (2014) Hydrodynamic alignment and assembly of nanofibrils resulting in strong cellulose filaments. *Nat Commun* 5:4018.
11. Torres-Rendon JG, Schacher FH, Ifuku S, Walther A (2014) Mechanical performance of macrofibers of cellulose and chitin nanofibrils aligned by wet-stretching: A critical comparison. *Biomacromolecules* 15:2709–2717.
12. Wu Y, et al. (2017) Bioinspired supramolecular fibers drawn from a multiphase self-assembled hydrogel. *Proc Natl Acad Sci USA* 114:8163–8168.
13. Zhao X (2017) Designing toughness and strength for soft materials. *Proc Natl Acad Sci USA* 114:8138–8140.
14. Kobayashi Y, Saito T, Isogai A (2014) Aerogels with 3D ordered nanofiber skeletons of liquid crystalline nanocellulose derivatives as tough and transparent insulators. *Angew Chem Int Ed Engl* 126:10562–10565.
15. Modulevsky D, Lefebvre C, Haase K, Al-Rekabi Z, Pelling A (2014) Apple derived cellulose scaffolds for 3D mammalian cell culture. *PLoS One* 9:e97835.
16. Martoïa F, et al. (2016) Cellulose nanofibril foams: Links between ice-templating conditions, microstructures and mechanical properties. *Mater Des* 104:376–391.
17. Usov I, et al. (2015) Understanding nanocellulose chirality and structure-properties relationship at the single fibril level. *Nat Commun* 6:7564.
18. Chen P, Ogawa Y, Nishiyama Y, Ismail AE, Mazeau K (2016) Linear, non-linear and plastic bending deformation of cellulose nanocrystals. *Phys Chem Chem Phys* 18:19880–19887.
19. Keckes J, et al. (2003) Cell-wall recovery after irreversible deformation of wood. *Nat Mater* 2:810–814.
20. Nishiyama Y, Langan P, Chanzy H (2002) Crystal structure and hydrogen-bonding system in cellulose Iβ from synchrotron X-ray and neutron fiber diffraction. *J Am Chem Soc* 124:9074–9082.
21. Leppänen K, et al. (2010) Small-angle x-ray scattering study on the structure of microcrystalline and nanofibrillated cellulose. *J Phys Conf Ser* 247:012030.
22. Diddens I, Murphy B, Krisch M, Müller M (2008) Anisotropic elastic properties of cellulose measured using inelastic X-ray scattering. *Macromolecules* 41:9755–9759.
23. Rusli R, Eichhorn SJ (2008) Determination of the stiffness of cellulose nanowhiskers and the fiber-matrix interface in a nanocomposite using Raman spectroscopy. *Appl Phys Lett* 93:033111.
24. Iwamoto S, Kai W, Isogai A, Iwata T (2009) Elastic modulus of single cellulose microfibrils from tunicate measured by atomic force microscopy. *Biomacromolecules* 10:2571–2576.
25. Pakzad A, Simonsen J, Heiden PA, Yassar RS (2012) Size effects on the nanomechanical properties of cellulose I nanocrystals. *J Mater Res* 27:528–536.
26. Dri FL, Hector LG, Moon RJ, Zavattieri PD (2013) Anisotropy of the elastic properties of crystalline cellulose Iβ from first principles density functional theory with van der Waals interactions. *Cellulose* 20:2703–2718.
27. Wu X, Moon RJ, Martini A (2011) Calculation of single chain cellulose elasticity using fully atomistic modeling. *Tappi J* 10:37–42.
28. Wu X, Moon RJ, Martini A (2013) Crystalline cellulose elastic modulus predicted by atomistic models of uniform deformation and nanoscale indentation. *Cellulose* 20:43–55.
29. Müller U, Sretenovic A, Gindl W, Teischinger A (2004) Longitudinal shear properties of European larch wood related to cell-wall structure. *Wood Fiber Sci* 36:143–151.
30. Wu X, Moon R, Martini A (2014) Tensile strength of Iβ crystalline cellulose predicted by molecular dynamics simulation. *Cellulose* 21:2233–2245.
31. Paavilainen S, et al. (2012) Mechanical properties of cellulose nanofibrils determined through atomistic molecular dynamics simulations. *Nord Pulp Pap Res J* 27:282–286.
32. Zugenmaier P (2008) *Crystalline Cellulose and Derivatives* (Springer, Berlin).
33. Hansen HS, Hünenberger PH (2011) A reoptimized GROMOS force field for hexopyranose based carbohydrates accounting for the relative free energies of ring conformers, anomers, epimers, hydroxymethyl rotamers, and glycosidic linkage conformers. *J Comput Chem* 32:998–1032.
34. Chen P, Nishiyama Y, Mazeau K (2014) Atomic partial charges and one Lennard-Jones parameter crucial to model cellulose allomorphs. *Cellulose* 21:2207–2217.
35. Ander P, Hildén L, Daniel G (2008) Cleavage of softwood kraft pulp fibers by HCl and cellulases. *Bioresources* 3:477–490.
36. Ogata S, Li J, Yip S (2002) Ideal pure shear strength of aluminum and copper. *Science* 298:807–811.
37. Ogata S, Li J, Hirosaki N, Shibutani Y, Yip S (2004) Ideal shear strain of metals and ceramics. *Phys Rev B* 70:104104.
38. Pokluda J, Černý M, Šandera P, Šob (2004) Calculations of theoretical strength: State of the art and history. *J Comput Aided Mater Des* 11:1–28.
39. Hearmon RS (1943) The significance of coupling between shear and extension in the elastic behaviour of wood and plywood. *Proc Phys Soc* 55:67–80.
40. Ferry JD, ed (1980) *Viscoelastic Properties of Polymers* (Wiley, New York).
41. Licup AJ, et al. (2015) Stress controls the mechanics of collagen networks. *Proc Natl Acad Sci USA* 112:9573–9578.
42. Calvetti F, Combe G, Lanier J (1997) Experimental micromechanical analysis of a 2D granular material: Relation between structure evolution and loading path. *Mech Cohesive Frict Mater* 2:121–163.
43. Rodney D, Gadot B, Riu Martinez O, Rolland Du Roscoat S, Orgéas L (2016) Reversible dilatancy in entangled single-wire materials. *Nat Mater* 15:72–77.
44. Albaret T, Tanguy A, Boioli F, Rodney D (2016) Mapping between atomistic simulations and Eshelby inclusions in the shear deformation of an amorphous silicon model. *Phys Rev E* 93:053002.
45. Bulatov V, Cai W, eds (2006) *Computer Simulations of Dislocations* (Oxford Univ Press, Oxford).
46. Hirth J, Lothe J (1982) *Theory of Dislocations* (Krieger Publishing Company, Malabar, FL).
47. Nishiyama Y (2018) Molecular interactions in nanocellulose assembly. *Philos Trans A Math Phys Eng Sci* 376:20170047.
48. Abraham MJ, et al. (2015) GROMACS: High performance molecular simulations through multi-level parallelism from laptops to supercomputers. *SoftwareX* 1–2:19–25.
49. Khazraji AC, Robert S (2013) Interaction effects between cellulose and water in nanocrystalline and amorphous regions: A novel approach using molecular modeling. *J Nanomater* 2013:409676.
50. Molnár G, Ganster P, Török J, Tanguy A (2016) Sodium effect on static mechanical behavior of MD-modeled sodium silicate glasses. *J Non-Cryst Solids* 440:12–25.
51. Goldhirsch I, Goldenberg C (2002) On the microscopic foundations of elasticity. *Euro Phys J E* 9:245–251.